Meta-aerogels: auxetic shape-memory polyurethane aerogels

Sadeq Malakooti[1,†], ABM Shaheen ud Doulah[2,†], Yao Ren[3], Vijay N. Kulkarni[3], Rushi U. Soni[2], Vaibhav A. Edlabadkar[2], Runyu Zhang[3], Stephanie L. Vivod[1], Chariklia Sotiriou-Leventis[2,*], Nicholas Leventis[2,4,*], Hongbing Lu[3,*]

[1] NASA Glenn Research Center, 21000 Brookpark Road, Cleveland, OH 44135, USA

[2] Department of Chemistry, Missouri University of Science and Technology, Rolla, MO 65409, USA

[3] Department of Mechanical Engineering, The University of Texas at Dallas, Richardson, TX 75080, USA

[4] Present address: Aspen Aerogels, Inc., 30 Forbes Road, Bldg B, Northborough, MA 01532, USA

[†] These authors contributed equally to the work.

[*] Corresponding authors: hongbing.lu@utdallas.edu, nleventis@aerogel.com, cslevent@mst.edu

Abstract. Shape-memory poly(isocyanurate-urethane) (PIR-PUR) aerogels are low-density monolithic nanoporous solids that remember and return to their permanent shape through a heating actuation step. Herein, through structural design at the macro scale, the shape-memory response is augmented with an auxetic effect manifested by a negative Poisson's ratio of approximately -0.8 at 15% compressive strain. Thus, auxetic shape-memory PIR-PUR monoliths experience volume *contraction* upon compression at a temperature above the glass transition temperature of the base polymer ($T_g \approx 30\ ^oC$), and they can be stowed indefinitely in that temporary shape by cooling below T_g. By heating back above T_g, the compressed/shrunk form expands back to their original shape/size. This technology is relevant to a broad range of industries spanning the commercial, aeronautical, and aerospace sectors. The materials are referred to as meta-aerogels and their potential applications include minimally invasive medical devices, soft robotics, and in situations where volume is at a premium, as for example for storage of deployable space structures and planetary habitats during transport to the point of service.

Keywords: shape memory, polymer, aerogel, auxetic, metamaterial, negative Poisson's ratio

1. Introduction

The shape-memory effect is a mechanical material property by which a material remembers and can be triggered to return to a permanent shape after it is deformed to and stored in a so-called temporary shape. The temporary-to-permanent shape transition is triggered by an external stimulus such as heat,[1] light,[2] humidity,[3] pH,[4] or electric and magnetic fields.[5] Shape-memory materials have many potential applications in medical technology,[6,7] implantable and wearable devices,[8,9] robotics,[10,11] and unassisted deployable structures aboard various aerospace platforms.[12,13] The typical trade-off in many of those applications is between mass density and mechanical strength. Yet lightweight, but at the same time high-toughness structural components are needed in applications ranging from delicate devices of interest to the reconstructive orthopedic surgery and implantable cardiovascular devices,[14–16] to large structures of interest to the aeronautical, and aerospace industries.[17] In that regard, thermally-triggered, shape-memory polymers, are particularly attractive.[18,19] One further refinement in the weight-to-performance ratio of shape-memory polymers was demonstrated recently by introducing polymeric shape-memory aerogels.

Aerogels are low-density three-dimensional nanostructured solids, mainly pursued for thermal insulation management in terrestrial, and aerospace, environments.[20–22] The “aero” part of the name “aerogel” points to the fact that they are prepared from wet gels by replacing their pore-filling solvent with air. This wet-gel origin of aerogels comprises their distinguishing difference from other aerogel-like micro- or nanocellular structures. In practice, the major concern during the drying process of wet gels is how to halt collapse of the skeletal framework during solvent removal; this is carried out by first replacing their pore-filling solvent with a low surface-tension liquid, such as liquid CO_2, which is then converted to a supercritical fluid that is vented off like a gas. The most well-studied class of aerogels is based on silica.[20,23,24] However, silica aerogels are notorious for their fragility, which limits the range of their applications. One way to address the fragility issue of oxide aerogels is to apply a conformal nano-thin polymer coating over their entire skeletal framework.[25–28] These materials are referred to as X-aerogels, and their strength-to-mass ratio renders them suitable even for ballistic protection (armor).[29–31] The topology of the nanoscopic composition of X-aerogels directed the rational design and development of purely polymeric aerogels from all major classes of polymers ranging from polyolefins,[32] phenolic resins including polybenzoxazines,[33] polyimides,[34] polyamides,[35] and polyureas,[36] to polyurethanes.[37–39] The latter class of aerogels includes recently reported rubber-like superelastic poly(isocyanurate-urethane) (PIR-PUR) aerogels that show a strong nanostructure-dependent shape-memory effect triggered by a temperature swing around their glass transition temperature.[40–42]

On the other hand, mechanical metamaterials exhibit auxetic physical properties such as negative Poisson's ratios,[43,44] the most striking manifestation of which is that under uniaxial compression they shrink instead of expanding in the transverse direction.[45] Such auxetic material designs have been utilized in biomedical devices, e.g., as artificial arteries, the wall thickness of which increases, rather than decreases, under the tension exerted during pulse-driven blood flow, thus enhancing the artery structural integrity, and thereby its lifespan.[46] Overall, materials with a negative Poisson's ratio tend to be more resilient to impact and indentation, and thus attractive for body armor technologies such as in bullet-proof helmets and vests.[47,48]

A large class of auxetic metamaterials comprises macroscopic structures based on blocks of rubber-like elastic polymers perforated through their bulk by a periodic arrangement of parallel tubes. i.e., tubes placed at regular intervals.[43,49] Since shape-memory polymeric aerogels are superelastic to begin with, it was reasoned that fabrication of such auxetic metastructures with polymeric aerogels that show the shape-memory effect would comprise a new class of materials, referred to herewith as meta-aerogels, which will be especially suitable as deployable panels in aerospace applications as they will contract and occupy less space during stowing in their folded temporary shape on their way to the location of their deployment in their permanent shape.

This concept is explored here with shape-memory PIR-PUR aerogels prepared via a sol-gel method with a commercial aliphatic isocyanurate-based triisocyanate (Desmodur N3300A), and triethylene glycol (TEG). The PIR-PUR sol was cast in suitable molds fabricated using 3D-printing of the negative of the computer-aided design (CAD) model of the metastructure of interest. After gelation and demolding, wet-gels were dried to monolithic meta-aerogels perforated with empty parallel tubes of the desired cross-sectional area, shape, and periodicity. Such meta-aerogels were programmed using a thermomechanical compressive load starting at a temperature above the glass transition temperature of the PIR-PUR aerogel. Expressing their negative Poisson's ratio, the PIR-PUR meta-aerogels shrunk under compression; then, while under load, meta-aerogels were cooled to a temperature well below their glass transition, thus fixing their temporary shape indefinitely. Meta-aerogels expanded quickly and recovered their original permanent shape via a heating actuation step back above their glass transition temperature.

2. Results and Discussion

2.1. Design and preparation of meta-aerogels

It is well-known that compressible polymeric blocks perforated with transverse parallel voids with specific cross-sectional shape running along the entire length of the blocks at regular intervals show auxetic properties and negative Poisson's ratios.[45,50] Recently, Bertoldi et al. studied the effect of the shape of the cross-section of the tubes on the compressive behavior of such 2D periodic structures and showed that the negative Poisson's ratios through buckling instabilities do depend on the cross-sectional shape of the tubes.[49] The cross-sectional shape of the tubes chosen for this work (Figure 1A – inset) was selected as the one with the most negative Poisson's ratio from the shapes investigated by Betroldi.[49] That auxetic structure was reconstructed using the SolidWorks 3D CAD software,[51] using a parametric function in polar coordinates with the center-to-center distance between neighboring holes set at $L_0 = 10$ mm; the total porosity due to the tubes was set at $\phi = 0.47$, and the number of repeat unit cells within the structure was set at $N = 8$. Other details for the design are given in Figure S.1 of Appendix I in Supporting Information. The design was implemented with additive manufacturing as described below.

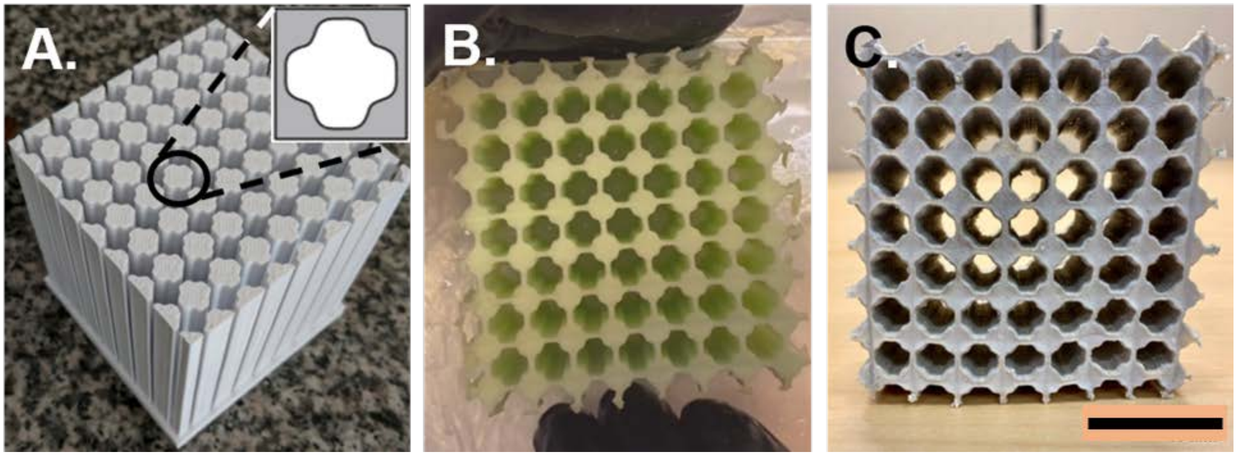

Figure 1. (A) Polylactic acid (PLA) mold: negative of the intended auxetic structure. The pillars become the periodic tubes with the cross-sectional shape shown as an inset. The side faces of the assembly were wrapped around with aluminum tape, and the sol was poured in from the top. (B) A poly(isocyanurate urethane) (PIR-PUR) wet gel right after demolding. The greenish color is due to the copper catalyst. (C) PIR-PUR meta-aerogel after washing and drying of the wet gel shown in (B). The scale bar in (C) is 2 cm.

Additive manufacturing and specifically desktop 3D printing techniques are emerging as a strong manufacturing tool for rapid prototyping of objects with complex geometries and topologies.[52,53] However, there are still limitations on the types of materials that can be 3D-printed directly. For example, we are not aware of any reports on 3D printed purely polymer aerogels.[54–57] Thus, the target design (Figures 1 and S.1) was prepared using 3D printing in conjunction with an inverse-molding process,[58] which has been utilized recently to prepare polyimide aerogel based materials with a LEGO brick shape.[59] Accordingly, the desirable meta-structure was used to guide the fabrication of a mold of its negative by subtracting the meta-structure from a solid body that envelops the entire meta-structure. All manipulations were carried out with the SolidWorks software. The mold is shown in Figure 1A. Details for the steps involved in this inverse molding technique, from design to fabrication, are provided in Figure S.2 of Appendix II in Supporting Information. The spikes in the mold that would eventually become the tubes perforating the meta-aerogel were held in place by the base of the mold, fabricated as an integral part with the spikes; eventually, that base plays the role of the bottom of the molding vessel during the molding process. The molding material for the spikes and the base was polylactic acid (PLA) printed in place directly using the fused-filament fabrication (FFF) method.[60] PLA is an extremely versatile molding material,[61] and it was chosen because it is not soluble in our acetonitrile-based sol (see below). The molding vessel was completed by wrapping the outer spikes (i.e., around their perimeter of the 3D-printed object) with aluminum tape. To facilitate demolding of our wet gels, all internal surfaces of the mold were spray-coated with a demolding agent (refer to the Experimental section). In case of more complex structures, the PLA mold can be removed by dissolving it away with dichloromethane using Soxhlet extraction.

Scheme 1. Synthesis of the aliphatic PIR-PUR material that comprises the basis for both the regular and the meta-aerogels of this report.

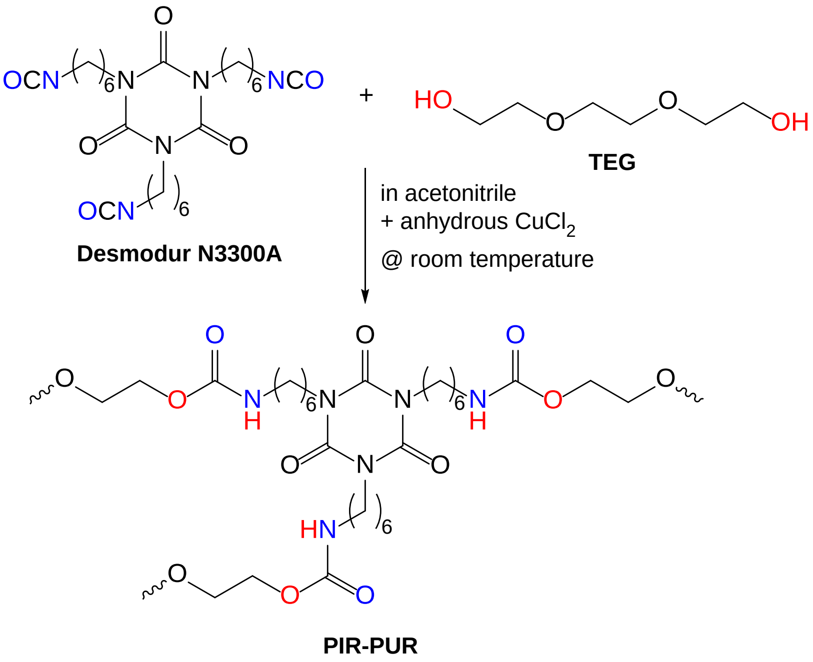

Adopted from our previous publication on ambient-pressure dried highly stretchable poly(isocyanurate urethane) aerogels,[42] the sol was prepared from an aliphatic isocyanurate-based triisocyanate (Desmodur N3300A) and triethylene glycol (TEG) mixed in their stoichiometric amounts (2:3 mol/mol, respectively) in acetonitrile at room temperature (Scheme 1). Unlike in our previous studies, the urethane forming reaction was catalyzed with anhydrous cupric chloride ($CuCl_2$) in 1:120 mol/mol ratio relative to the triisocyanate. The exact formulations are tabulated in Table S.1 of Appendix III in Supporting Information. The choice of $CuCl_2$ as the catalyst, over the more conventional dibutyltin dilaurate (DBTDL), was based on the fact that it was found to be much more active than the latter for the urethane forming reaction of Scheme 1; in turn, that allowed shortening of the gelation time and facile creation of gels and aerogels with bicontinuous micromorphologies that are much stiffer than the spheroidal structures produced by slower gelation with DBTDL.[41] Stiffer materials can store more energy for a given deformation, which was deemed essential for auxetic structures, which, by design, contain less material, because of the tubular voids that render the material auxetic in the first place. For meta-aerogels, stiffer aerogel structures are highly desirable, because, all other factors being equal, at a given strain they can store more energy with less mass. By being less dense by design relative to their simple shape-memory counterparts, meta-aerogels can utilize every bit of extra stored energy for shape recovery.

The sol was poured into the molds and the whole assembly was wrapped with parafilm. Gelation took place within 5 min and the resulting gels were aged in their molds for 1.5 h. Wet gels were then removed from the molds into acetone (Figure 1B). The greenish color was due to the copper catalyst. After four acetone washes and four pentane washes (24 h each time at room temperature), the pentane-filled wet-gels were let to dry for 24 h at room temperature; drying was completed at 50 ^{o}C for 5 h. (CAUTION: pentane-filled wet gels are a fire/explosion hazard. Drying from pentane has to be carried out in a well-ventilated fume hood at room temperature.) A dry meta-aerogel is shown in Figure 1C. Sometimes, minor defects introduced during demolding might be observed around the edges of the structure. The auxetic/shape-memory performance, however, as it is described in Section 2.4, remained unaffected.

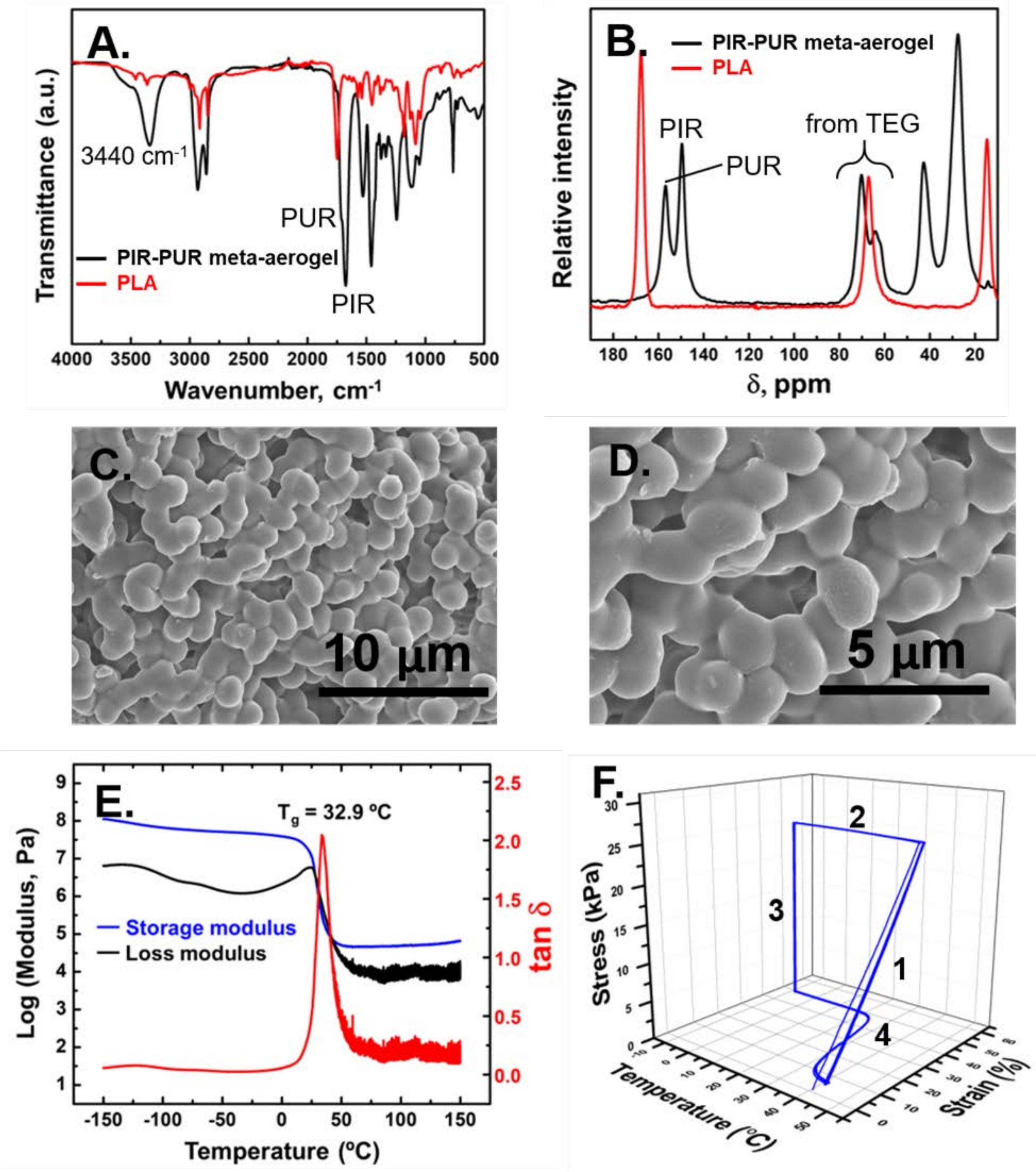

Figure 2. (A) FTIR spectrum of a meta PIR-PUR aerogel. (B) Solid-state CPMAS ^{13}C NMR spectrum of a meta PIR-PUR aerogel. The red-line spectra in frames (A) and (B) are those of polylactic acid (PLA – the mold material) showing the absence of cross-contamination. "PIR" refers to features assignable to the isocyanurate ring, and "PUR" to features assignable to urethane. (C, D) SEM image of the PIR-PUR aerogel matrix at two different magnifications showing that the microstructure is bi-continuous. (E) Dynamic mechanical analysis (DMA) at 1 Hz of a PIR-

PUR aerogel as a function of the temperature for the determination of the glass-transition temperature (T_g = max tan δ = 32.9 ºC). (F) Five thermomechanical cycles of a PIR-PUR aerogel showing the shape-memory effect (see Section 2.2). After the first cycle the sample became slightly stiffer; the traces from cycles No. 2 to No. 5 coincide.

2.2. Materials characterization

The PIR-PUR aerogels were chemically characterized using Fourier-transform infrared spectroscopy (FTIR – Figure 2A), and solid-state CPMAS ^{13}C NMR (Figure 2B). The corresponding spectra of PLA are included with red lines, showing no cross-contamination from the molds. The FTIR spectra were dominated by the isocyanurate carbonyl stretch at 1680 cm^{-1}. The 2300–2000 cm^{-1} region was clean of any unreacted N=C=O stretch. The free urethane carbonyl stretch was observed as a 1729 cm^{-1} shoulder to the intense isocyanurate absorption. Possible hydrogen-bonded urethane carbonyl stretches would appear in the 1600-1640 cm^{-1} region, and they were masked by the intense isocyanurate absorption. Methylene ($-CH_2-$) in-plane bending was observed at 764 cm^{-1}.[62] The urethane N-H stretch was observed as a medium-intensity peak at 3440 cm^{-1}. N–H bending coupled to C–N stretching gave an absorption at 1530 cm^{-1}.[63] The absorptions at 1244, 1120, and 1048 cm^{-1} were attributed to the triethylene glycol and urethane asymmetric and symmetric C–O–C stretches.[63,64] In cross-reference to Scheme 1, the resonances in the 14-44 ppm region of the solid-state ^{13}C NMR spectrum correspond to the CH_2 carbons coming from Desmodur N3300A. Resonances between 60 and 80 ppm came from the CH_2 groups of TEG. The sharp resonance at 149 ppm corresponds to the carbonyl carbon of the isocyanurate ring. The peak at 156 ppm is attributed to the carbonyl carbons of the urethane groups.[65] In agreement with the FTIR spectrum, no peak corresponding to unreacted N=C=O was detectable.

Microscopically, the PIR-PUR meta-aerogels of this study are classified as bicontinuous materials frozen at an early stage of spherulization along a spinodal-decomposition gelation process (see Figures 2C and 2D), as the plan was by adopting anhydrous $CuCl_2$ as the catalyst. With a more conventional gelation catalyst like DBTDL, the same sol composition yields similar-density materials with spheroidal morphologies.[42]

Bulk material properties of PIR-PUR aerogels and PIP-PUR meta-aerogels are summarized and compared in Table 1. Both PIR-PUR aerogels and meta-aerogels undergo similar linear shrinkages relative to their molds (about 25-27%). The entire shrinkage for both types of samples occurred only during their drying process. The skeletal density was common for both types of samples (1.23 ± 0.002 g/cm^3), and their bulk densities were calculated from their weight and physical dimensions. The bulk density of the PIR-PUR aerogels at the current monomer concentration was 0.33 g/cm^3 with porosity equal to 73.5 % v/v. As-prepared meta-aerogel samples had a lower density (0.18 g/cm^3), and correspondingly a higher porosity (85.4 % v/v).

Table 1. Material properties of PIR-PUR aerogel and meta-aerogel samples.

Name	Linear Shrinkage (%)	Porosity (%) [a]	Bulk Density (ρ_b, g/cm^3)	Storage Modulus (kPa) [d]	Loss Modulus (kPa) [d]
PIR-PUR Aerogel	24.5 [b]	73.5	0.33	292	79.4
PIR-PUR Meta-aerogel	26.6 [c]	85.4	0.18	11.9	2.74

[a] Porosity = 100×[($\rho_s - \rho_b$) / ρ_s]. The Skeletal Density (ρ_s) of both types of aerogels was 1.23 ± 0.002 g/cm^3.

[b] Linear Shrinkage = 100×[(Mold diagonal – Sample diagonal) / Mold diagonal].

[c] Linear Shrinkage = 100×[(Mold length – Sample length) / Mold length].

[d] Using dynamic mechanical analysis (DMA) in compression at 50 ºC with excitation frequency = 1 Hz.

The glass transition temperature of the PIR-PUR aerogel material was determined with dynamic mechanical analysis (DMA) in tension. Figure 2E shows the variation of the storage and loss moduli (G’ and G”, respectively), as well as of tan δ (= G”/G’) of a PIR-PUR aerogel sample at 1 Hz as a function of temperature. At low temperatures, the storage modulus was about 100 times higher than the loss modulus; as the temperature increased, the values of both moduli decreased, and crossed one another. Eventually, at the high-temperature plateau G’≈10 G”. The glass transition temperature, T_g, of the PIR-PUR aerogel was determined as the peak of tan δ (32.9 °C). This value was used to set the range for the appropriate T_{high} and T_{low} temperatures during the shape-memory thermomechanical cycling. Thus, it was noted that the low-modulus state started to get stabilized at about 40 °C, and T_{high} was set equal to that temperature. Correspondingly, T_{low} was set at -10 °C, i.e., about 40 °C lower than T_g. The inherent shape-memory capability of the PIR-PUR aerogels was confirmed with thermomechanical cycling between T_{high} and T_{low} as shown in Figure 2F. In the beginning, an as-prepared (i.e., previously unstretched) sample was first equilibrated at T_{high} = 40 °C for 5 min. Then, in Stage 1 of the curve in Figure 2F, the sample was stretched near its yield strain (60%). At that point (Stage 2 in Figure 2F), the load (stress) was kept constant while the temperature was reduced at 5 °C/min to T_{low} (-10 °C). Subsequently, in Stage 3, the sample was unloaded isothermally (at -10 °C). Finally, in Stage 4, strain recovery was recorded while the temperature was increased to T_{high} (at 1 °C/min). After a 15 min isothermal hold at T_{high}, the cycle was repeated another 4 times. In agreement with our previous findings based on similar aerogels with a spheroidal morphology,[40,41] in the second cycle and beyond the sample settled, becoming stiffer (modulus = 131 kPa), and all thermomechanical curves coincided with one another. Previous stress-relaxation experiments of the same PIR-PUR base material (made with a different catalyst at different morphologies) at T_g + 40 °C, at T_g and at T_g – 40 °C, in conjunction with ATR-FTIR have shown that settling after the first heating-stressing cycle is accompanied by maximization of the H-bonding interactions of the NH group with the carbonyl groups along the backbone and the glycol groups from TEG.[40,41] Various projections of the 3D data of Figure 2F on the planes of the figure are shown in Figure S.3 of Appendix IV in Supporting Information. Those projections allow calculation of the figures of merit of the shape-memory effect (see Table S.2 of Appendix IV in Supporting Information). These figures of merit were found similar to those reported in our previous studies:[40,41] Strain Fixity Ratio ~ 99%; Strain Recovery Ratio ~ 80%; Strain Recovery Rate ~ 5 min^{-1}; and, the overall Fill Factor ~ 59%.

2.3 Deep rubbery-state viscoelastic properties of PIR-PUR and meta-PIR-PUR aerogels

As a preamble to the thermomechanical testing of the meta-aerogels, we looked at the equivalency of the PIR-PUR aerogels in their regular versus auxetic forms (i.e., perforated with tubes as shown in Figure 1C). For this, we looked at the effect of the auxetic structure on the dynamic behavior in the frequency domain of the meta-aerogels in comparison with straight PIR-PUR aerogels in a deep rubbery state (at 50 ^{o}C, i.e., well above T_g) where the short-range interactions of the polymer chains are vanishing. Accordingly, the viscoelastic properties of the PIR-PUR aerogel and the meta-aerogel samples were measured in the compression mode using Dynamic Mechanical Analysis (DMA) carried out with an Instron ElectroPuls E10000 load frame equipped with an environmental chamber as described in the Experimental Section. Using the cyclic displacement control mode, the samples were tested at 1% compressive strain offset with 0.1% oscillatory strain amplitude at different frequencies. Figure 3 compares the viscoelastic properties of the PIR-PUR aerogels and of the meta-aerogel samples at different frequencies. Both samples were held at least for 45 min at the target temperature to reach equilibrium conditions, then the steady-state response (load) to the harmonic excitation (displacement) was measured. The general trends in storage moduli of both aerogel and meta-aerogel samples were similar. The storage modulus increased monotonically with frequency. However, meta-aerogel samples were much softer than the aerogel sample due to the inclusion of the macroscopic tubular voids (e.g., the low-frequency storage modulus of the meta-aerogel was an order of magnitude lower than the aerogel's corresponding value). On the other hand, the loss modulus of both samples was non-monotonic with respect to frequency. This is in contrary to what is expected for glassy polymers, in which, typically, the loss modulus decreases monotonically with increasing frequency. It is speculated that in their rubbery state (i.e., above T_g as the case is here), it is more likely to excite high-frequency dissipative modes leading to the observed non-monotonic behavior for the loss modulus spectrum.[66] The loss moduli of both the PIR-PUR aerogel and of the meta-aerogel converged at the high-frequency region (above 10 Hz). This behavior was only seen for the loss modulus, and therefore the tan δ of the meta-aerogel surpassed the corresponding values for the straight aerogel sample. Such a structure-dependent dynamic behavior points to the need for further studies of the dynamic properties as a function of different meta-structure parameters such as wall thickness and pore size. Those studies fall beyond the scope of this report, however, it can be concluded safely that for the present comparison at the quasi-static frequency domain (frequency→0), meta-aerogels and straight aerogels are equivalent materials.

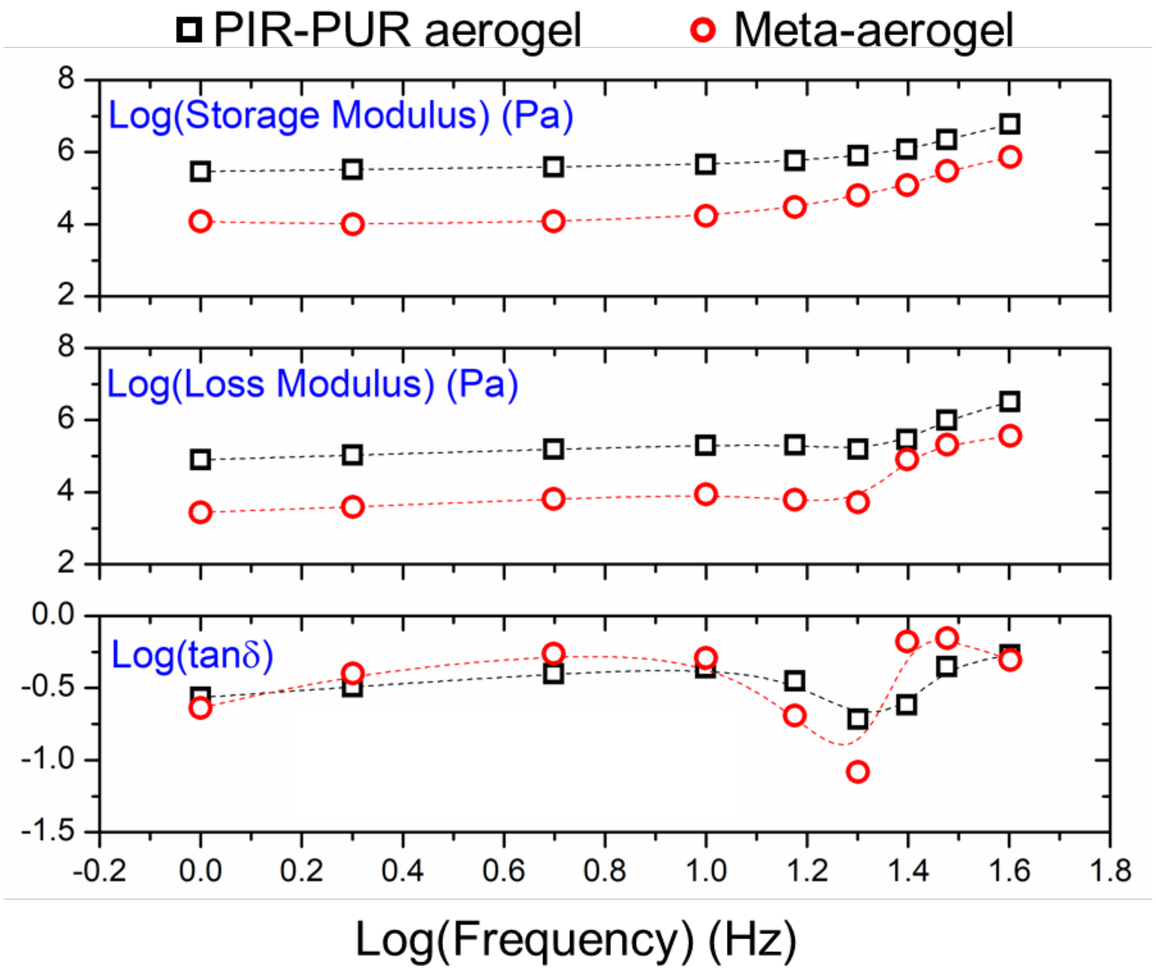

Figure 3. Viscoelastic properties in compression of straight and meta-aerogel PIR-PUR samples in their rubbery state (50 ^{o}C) as indicated.

At the end, after cyclic loading at 50 ^{o}C for approximately 2000 cycles, the meta-aerogel sample was scanned using a Nikon 225 kV X-ray micro-computed tomography (CT) system, in order to investigate the presence of any damage (e.g., development of cracks). No obvious defects were observed in the meta-structure, pointing to the durability and resilience of those samples under these loading conditions. Movie S1 in Supporting Information shows cross-sectional slices of the CT scanned volumetric image of the meta-aerogel sample.

2.4. Auxetic behavior superimposed with the shape-memory effect

Owing to the specific meta-structure design that was implemented in this work, the auxetic behavior of the resulting PIR-PUR meta-aerogels was visible only in compression. Thereby, the shape-memory characteristics of the meta-aerogel were recorded through a shape-memory thermomechanical cycle analogous to the one of Figure 2F, but in the compression mode instead. Testing was carried out with the same Instron ElectroPuls E10000 load system used for the study of the viscoelastic properties in Section 2.3, and a pre-conditioned meta-aerogel sample, 58.21 mm × 30 mm × 25.4 mm in size, cut from a larger sample similar to the one shown in Figure 1C. Thermomechanical data are shown in Figure 4A. T_{high} and T_{low} were set to 50 °C and 5 °C, respectively. In the beginning, the meta-aerogel sample was heated to 50 °C and was equilibrated for 15 min. Then, in Stage 1, the sample was compressed isothermally to -15% strain, showing a strong auxetic behavior exemplified by progressive contraction in the middle as strain increased (see Movie S2 in Supporting Information). Next, in Stage 2, the stress was kept constant while the temperature was lowered to T_{low} and the sample was equilibrated at that temperature for 30 min. In Stage 3, the meta-aerogel was unloaded, and could remain in the laterally-contracted auxetic shape indefinitely (see the first frame on the top of Figure 4B). Finally, in Stage 4 the sample was heated back to T_{high} (0.5 °C s^{-1}). Movie S3 in Supporting Information shows the recovery of the meta-aerogel from the programmed auxetic shape at -15% strain to its undeformed configuration at $T_{\mathrm{high}} = 50\ ^{\mathrm{o}}\mathrm{C}$. Snapshots of the meta-aerogel during Stage 4 were taken every 5 s, and were used to record the strain during shape recovery. Selected such snapshots during strain recovery are shown in Figure 4B.

The quality of the shape-memory effect of the meta-aerogel was evaluated via the same figures of merit used for the evaluation of that effect in the regular (not auxetic) PIR-PUR aerogels (see Section 2.2). Data analysis used to evaluate these figures of merit for the meta-aerogel are included in Figure S.3, and values are listed in Table S.2 of Appendix IV in Supporting Information. The Strain Fixity Ratio of the meta-aerogel (99.3%) was practically equal to that of the straight PIR-PUR aerogels. However, both the Strain Recovery Ratio (~98%) and the Strain Recovery Rate (~ 15 min^{-1}) of the meta-aerogel were found significantly higher that the values calculated for the straight PIR-PUR aerogels (~80% and 5 min^{-1}, respectively), which is reflected to a higher value for the overall figure of merit: Fill Factor of the meta-aerogel = 0.69, versus 0.59 for the straight PIR-PUR aerogels. From another perspective though, upon closer inspection of the strain recovery versus temperature plots of Figures S.4C and S.4.D of the straight versus the meta-aerogels, respectively, one notices that the recovery of the meta-aerogel starts at about 11-12 ^{o}C, that is well below the glass transition temperature of the PIR-PUR material, while the regular aerogel samples start recovering their shape at the vicinity of their glass transition temperature. Furthermore, interestingly, at that lower-temperature range where meta-aerogels start recovering their shape, the strain values move rapidly through the range: (a) in which there is a hump in the stress-strain curve during isothermal compression in Stage 1 (that hump is pointed at with a yellow arrow in Figure 4A), and (b) that roughly corresponds to the strain range where all tubes have collapsed under compression (refer to Movie S2 in Supporting Information). Therefore, the early onset of the meta-aerogel shape recovery must be linked to the meta-structure. In that regard, it is reasonable to assume that at low-temperatures both the short- and the long-range interactions between the polymeric segments are at their lowest energy states. According to the data then, short-range polymeric interactions, which are involved primarily in the material's intrinsic shape memory capability, are activated at higher temperatures – closer to T_g. On the other hand, however, long-range polymer interactions must be activated at temperatures well below the glass transition temperature. During the shape-recovery stage of the meta-aerogels, the long-range polymer interactions are activated first, turning the meta-aerogel from a stress-free state into a stressed one. Thereby the initial recovery is due to the fact that the meta-aerogel sample is first releasing its elastic energy stored in the meta-structure (post hump in Figure 4A), and thus reaches a new stress-free state similar to that in the regular PIR-PUR aerogels. By further increasing the temperature, the short-range interactions are coming into play, and finally the meta-aerogel recovers its original shape. Clearly, the initial low-temperature / high-strain spring-back effect in the meta-aerogel recovery process does not exist in the regular PIR-PUR aerogels.

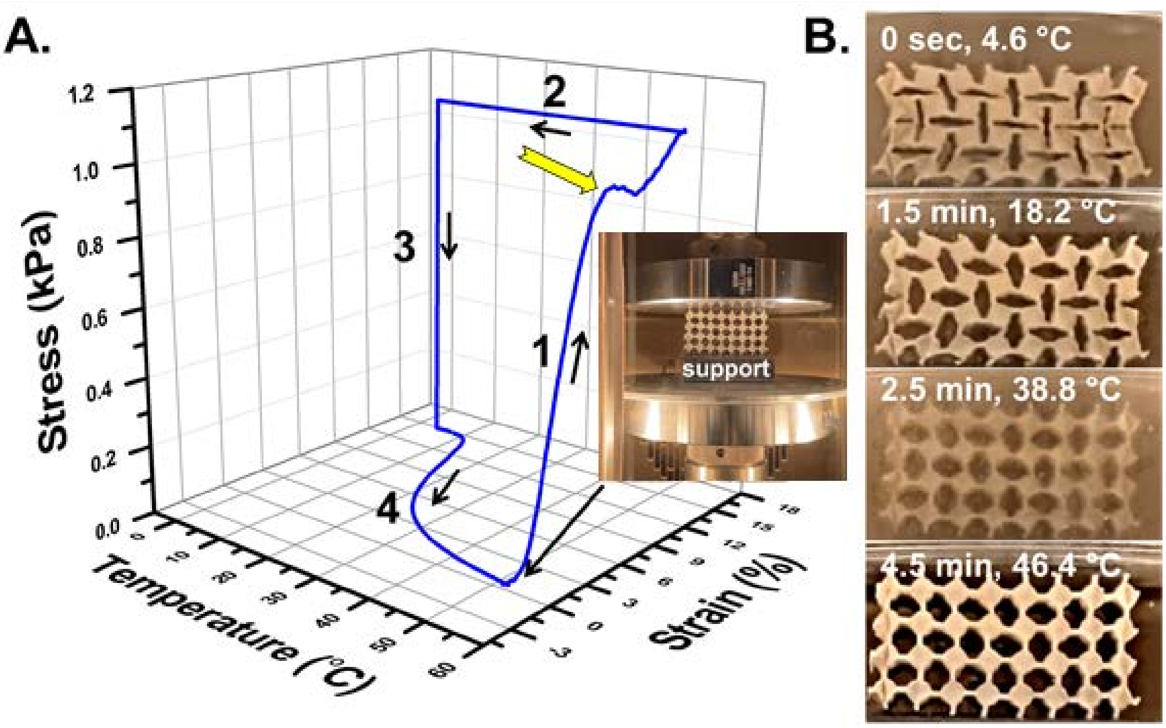

Figure 4. (A) A thermomechanical cycle of a preconditioned meta-aerogel sample. Stage 1: compression to -15% strain at the deformation temperature $T_{\text{high}} = 50\ ^{\text{o}}\text{C}$; Stage 2: cooling under constant stress to fixing temperature $T_{\text{low}} = 5\ ^{\text{o}}\text{C}$; Stage 3: stress release at T_{low}; and, Stage 4: shape recovery by heating back to T_{high} ($0.5\ ^{\text{o}}\text{C s}^{-1}$). Inset: experimental set up at the beginning of the cycle. Yellow arrow points to a hump along the stress-strain curve discussed in the text. (B) Snapshots along shape recovery (Stage 4).

In terms of quantifying the auxetic effect, at first, Figure 5A takes a closer look at the temperature stimulus applied to the meta-aerogel along with the axial and transverse strains of the meta-aerogel as a function of time during the last stage (Stage 4) of the thermomechanical cycle of Figure 4A. In reference to Figure 5B, the axial strain (ε_y) is defined as $\varepsilon_y = (l - l_0)/l_0$ and the transverse strain (ε_x) is given by $\varepsilon_x = (w - w_0)/w_0$. It is noted that these strain definitions are global and different from their corresponding values at local material points. The axial strain history follows the temperature stimulus almost precisely, thus showing that meta-aerogels are very responsive, which is important for applications in actuation.

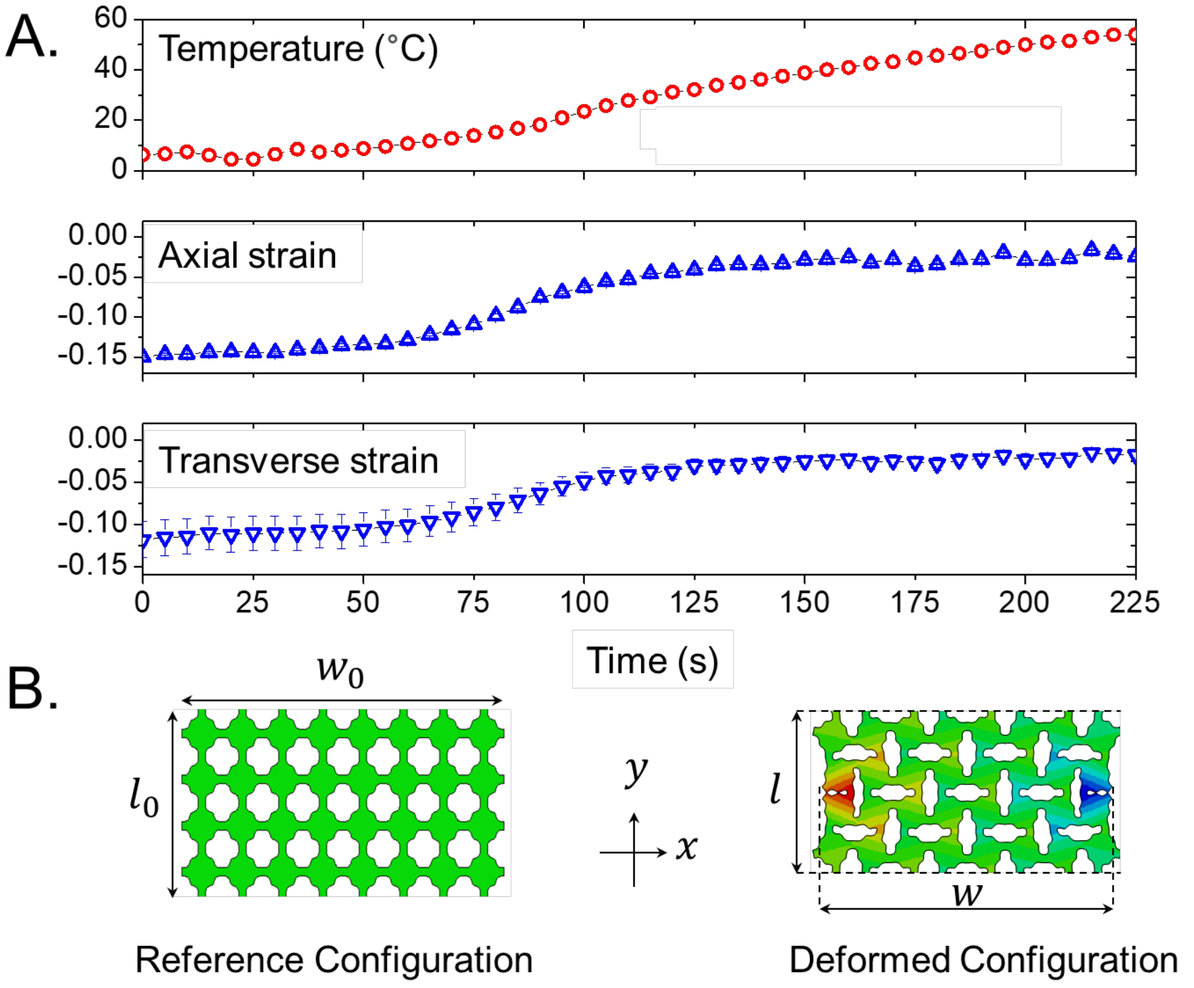

Figure 5. (A) Temperature, axial strain, and transverse strain as a function of time during the last stage (Stage 4) of the shape-memory thermomechanical cycle of Figure 4A; (B) Reference and deformed configurations of the meta-aerogel, and definitions relevant to the determination of the Poisson's ratio (see text).

Following our global definitions for the axial and transverse strains, the Poisson's ratio then becomes $\nu = -\varepsilon_x/\varepsilon_y$. Figure 6A shows the Poisson's ratio of the meta-aerogel sample as a function of the axial strain during the initial isothermal compression stage at 50 °C (Stage 1) as well as during the shape recovery stage (Stage 4). During Stage 1, the Poisson's ratio shows a sigmoidal decay from a value slightly above zero (Poisson's ratio of about 0.05 at strains less than -1%) to a Poisson's ratio of approximately -0.8 at -15% compressive axial strain. However, during the shape recovery stage (Stage 4), the Poisson's ratio of the meta-aerogel did not recover to a positive value. This is related to the residual strain due to rearrangement of the H-bonding relationships within the PIR-PUR aerogels as discussed in conjunction with the settling observed between the first and the subsequent cycles of the shape-memory experiment of Figure 2F.[40] For reference, the Poisson's ratio of the meta-aerogel as a function of temperature during Stage 4 is shown in Figure 6B.

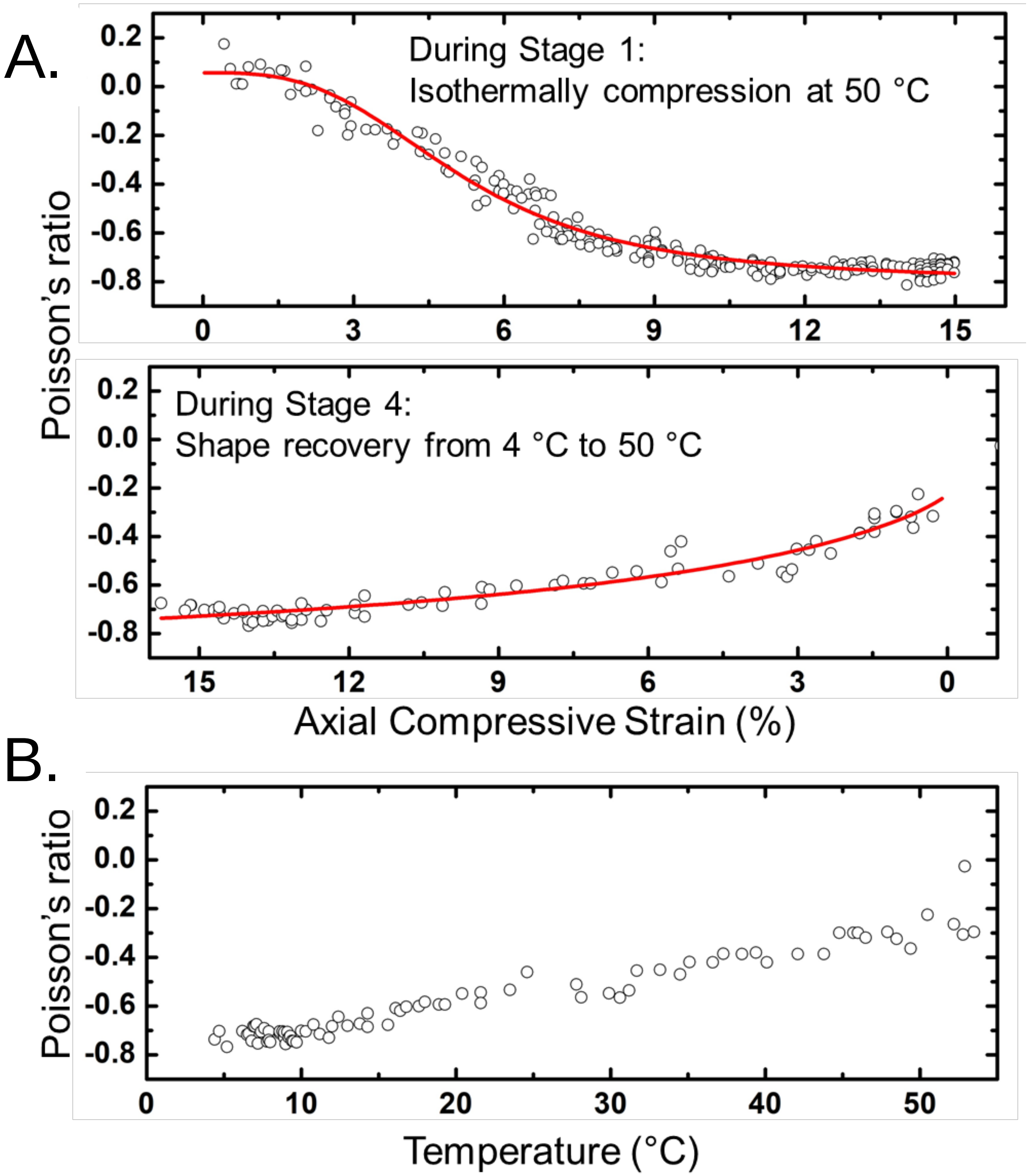

Figure 6. (A) The Poisson's ratio of the meta-aerogel sample as a function of compressive axial strain during Stage 1 and Stage 4 of the shape-memory thermomechanical cycle. The solid red line is the best-fit curve. (B) The Poisson's ratio of the meta-aerogel sample as a function of temperature during Stage 4 of the shape-memory thermomechanical cycle of Figure 4A.

Finally, the fact that the auxetic effect of meta-aerogels originates from their molded meta-structures was further supported by comparing the experimental Poisson's ratio results during Stage 1 (Figure 6A) with simulation results obtained from a 2D linearly elastic finite element method (FEM) using the commercially available finite element code ABAQUS. The effect of viscoelastic properties on the Poisson's ratio was not considered in these simulations, thus leaving only the tubes as the only relevant parameter for the auxetic effect. Figure 7 compares the evolution of the experimental and numerical Poisson's ratios as a function of compressive strain. Despite the lack of any viscoelastic material property considerations, the FEM simulation predicted the experimental results well; in fact, at high strains, i.e., where the auxetic effect is most relevant, the FEM simulations and the experimental results were in excellent agreement. Small deviations between the experimental and simulation results were observed at small strains (less than 0.05). The simulations assume a perfect geometry, but in practice, the presence of small defects introduced during manufacturing process could potentially cause the slight discrepancies. However, their consistent trend at low strains and perfect matching at high strains clearly indicate the major role of the metastructure on the global behavior of the meta-aerogels.

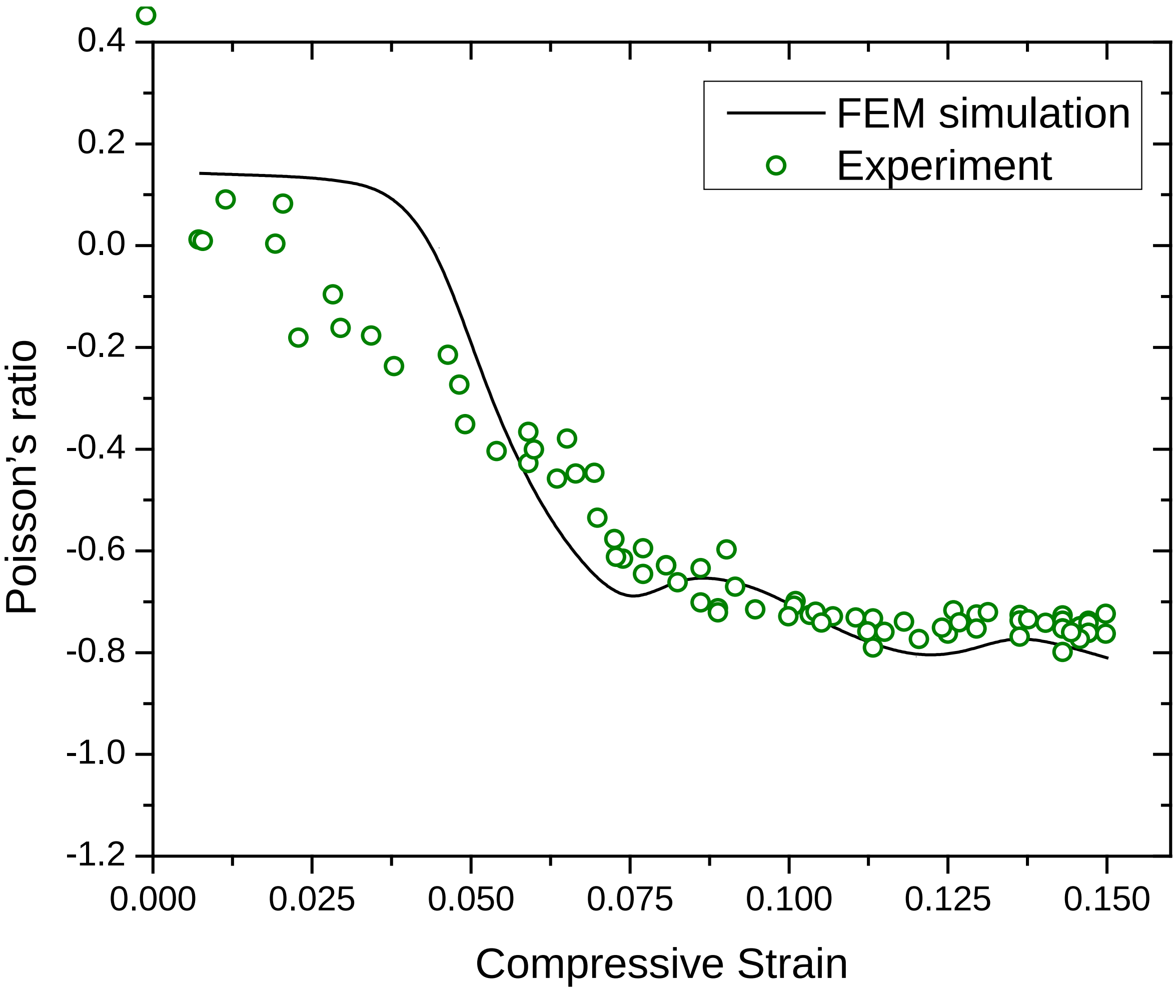

Figure 7. Experimental versus simulated results for the evolution of the Poisson's ratio of meta-aerogels as a function of compressive strain.

3. Conclusion

Meta-aerogels combine a negative Poisson's ratio with a thermoresponsive shape-memory effect, and they are potentially important materials for commercial, aeronautical, and aerospace applications. Upon cooling well below T_g, meta-aerogels maintain the auxetic shape at their shrunk/negative Poisson's ratio state that was imposed on them by compression at a temperature above T_g, and upon heating back above T_g they recover their original configuration. The particular aerogel material that was used for demonstrating those effects was based on a highly cross-linked poly(isocyanurate urethane) polymeric backbone and the auxetic form was achieved with parallel tubular voids running the length of a macroscopic block of a standard aerogel of that material. The Poisson's ratio reached -0.8 at -15% compressive strain. The shape recovery of those meta-aerogels traced a temperature increase as fast as 0.5 ^{o}C/s. These materials comprise a good platform for further exploration of applications of additive manufacturing through molding techniques in the fabrication of functional aerogels. In terms of possible future designs, exploration of tubes with different cross-sectional shapes is a possible route for further study, while totally different 3D designs of shape-memory aerogels perforated with multi-dimensional tube designs are also possible candidates for further investigation.

4. Materials and methods

Materials

All materials were commercially sourced and used without further processing. Desmodur N3300A triisocyanate was generously donated in pure form by Covestro LLC (Pittsburg, PA). Triethylene glycol (TEG), anhydrous acetonitrile, and anhydrous $CuCl_2$ were purchased from Fisher Scientific (Hampton, NH).

Synthesis of PIR-PUR regular and meta-aerogels

In a typical synthetic procedure, 30 mmol of Desmodur N3300A and 45 mmol of TEG were dissolved in 207.80 mL of anhydrous acetonitrile (refer to Table S.1 of Appendix III in Supporting Information). The solution was stirred for 10 min at room temperature. A catalyst stock solution was prepared by dissolving 2.789 g of anhydrous $CuCl_2$ in 250 mL of acetonitrile. Then, 5.6 mL of the catalyst stock solution was added to the reaction mixture. The resulting solution was stirred for another 5 min and was poured into the appropriate molds. For regular aerogels the molds were 25 mL plastic vials. For the meta-aerogels, the design of the molds is described in Figures S.1 and S.2 of Supporting Information. The meta-aerogel mold design was the negative of the desirable meta-aerogel structure, and it was submitted in the STL (Standard Triangle Language) format to 3D Hubs, an online manufacturing platform[67] to be 3D printed with polylactic acid (PLA) with 100 μm resolution and 30% infill percentage. The spikes of the mold protruded out and were an integral part of a PLA base that eventually played the role of the bottom of the gelation container. The mold was completed by wrapping the outer spikes around with aluminum tape. The entire inner surface of the mold was sprayed with a mold release spray (Sprayon MR™311, Cleveland, OH). Wet gels were aged inside the molds for 1.5 h. After aging, wet gels were removed from the molds and were washed with anhydrous acetone (4 times, 24 h each time), and finally they were washed with pentane (4 times, 24 h each time). In our current two-dimensional meta-aerogel design as shown in Figure 1, wet-gels were removed from their molds by lifting the bottom side of the wet-gel and unplugging it from the mold. The amount of solvent used for each washing step was equal to four times the volume of the wet gel. Pentane-washed wet gels were dried under ambient conditions for 24 h. Drying was considered complete after placing the samples in an oven at 40 °C for 3 h.

Chemical characterization

Attenuated total reflectance (ATR) FTIR spectroscopy was carried out with a Thermo Scientific Nicolet iS50 FT-IR, equipped with an ATR accessory. Samples were cut to the size of the ATR diamond crystal, and ATR-FTIR spectra were obtained by pressing them against the crystal with the ATR unit's pressure device (gripper).

Solid-state CPMAS ^{13}C NMR spectra were obtained with powdered samples on a Bruker Avance III 400 MHz spectrometer with a carbon frequency of 100 MHz using a 7 mm Bruker MAS probe at a magic angle spinning rate of 5 kHz, with broadband proton suppression, and the CP TOSS pulse sequence. The Total Suppression of Spinning Sidebands (TOSS) pulse sequence was applied by using a series of four properly timed 180° pulses on the carbon channel at different points of a cycle before acquisition of the FID, after an initial excitation with a 90° pulse on the proton channel. The 90° excitation pulse on the proton and the 180° excitation pulse on carbon were set to 4.2 and 10 μs, respectively. A contact time of 3 ms was used for cross-polarization. Solid-state ^{13}C NMR spectra were referenced externally to glycine (carbonyl carbon at 176.03 ppm). Chemical shifts reported versus TMS (0 ppm).

Physical characterization

Bulk densities (ρ_b) were determined from the weight and the physical dimensions of the samples. Skeletal densities (ρ_s) were determined with helium pycnometry using a Micromeritics AccuPyc II 1340 instrument. Porosities (Π) as a percent of empty space were determined from the ρ_b and ρ_s values via $\Pi = 100 \times [(\rho_s - \rho_b)/\rho_s]$.

Scanning electron microscopy (SEM) was conducted with Au/Pd (60/40) coated samples on a Hitachi Model S-4700 field emission microscope. The sample was placed on the stub with Cdot. Thin sticky Cu stripes were cut and placed on the edges and top of the sample leaving a small area uncovered for observation.

Micro-computed tomography scans were carried out using a Nikon Microfocus 225 kV X-ray source. The effective pixel resolution was 50 μm/pixel. The X-ray projection images were obtained through rotating the frame around the center of the sample, and using the Nikon computer software, these projection images were converted into a 3D object. The 3D object was later sliced using the free-academic-licensed software Dragonfly to reveal the internal structure of the sample.

Thermomechanical characterization

The glass-transition temperature (T_g) of the PIR-PUR aerogel material was determined using a TA Instruments Q800 dynamic mechanical analyzer (DMA) in the tension mode performing a dynamic ramp at 1 Hz from −150 °C to 150 °C at 3 °C min^{-1}. Thermo-mechanical cycling of regular PIR-PUR aerogels was conducted in tension using the same DMA instrument in the controlled-force mode as follows: samples were equilibrated at their deformation temperature (T_{high} = 40 ^{o}C) for 5 min. Then they were stretched with a small tensile force (0.01 N), and the length of the sample was measured by the instrument and stored. Next, specimens were stretched at a constant force rate of 1 N min^{-1} up to near their break point (typically around 60% strain), and then, while under the final stress, they were cooled at 5 °C min^{-1} to the fixation temperature (T_{low} = -10 ^{o}C ≪ T_g). Samples were equilibrated at T_{low} for 5 min, and the tensile force was reduced to 0.01 N. Samples were allowed to relax (fix) for 15 min (always while at T_{low}) while strain was recorded. Finally, samples were heated at 1 °C min^{-1} to their recovery temperature (T_{high} = 40 ^{o}C) while strain was still recorded. Samples were held at T_{high} for 15 min, and the cycle was repeated. Five such cycles were run successively for each sample.

Thermomechanical cycling of auxetic meta-aerogels (nominal size of 58.21 mm × 30 mm × 25.4 mm) was performed in the compression mode on an Instron mechanical testing system (Instron Inc., Electropuls E10000 load frame, Norwood, MA) equipped with a 500 N load cell (with an accuracy of 0.5% of the reading), and an Instron Environmental Chamber (Instron, Inc., Model 5969, Norwood, MA). During the first and last step (Figure 4A, Stages 1 and 4), the sample was monitored continuously with a Nikon camera (Model D7100) kept at a fixed position normal to the sample (see Movies S2 and S3). During Stage 4, the camera was also recoding simultaneously the temperature of the sample by placing the display of our thermal couple next to the Environmental Chamber (see Movie S3). The bottom part of Figure 4A (strain versus temperature during shape recovery) was constructed by taking a series of digital images every 5 s from Movie S3 like those shown in Figure 4B. The images were analyzed using the open-source image-processing package, ImageJ. For this, the total absolute area of the holes was measured in each digital image, and was divided by the total area of the holes before any compression (from Movie S2). The strain at each time interval / temperature was set equal to the square root of each area ratio. Poisson's ratios were also measured from the digital images using ImageJ by comparing the dimensions of the sample at different stages of deformation with corresponding values for the undeformed sample before compression (see Figure 5B). Samples were equilibrated at each target temperature for at least 15 min before moving to the next step. Deep rubbery state DMA measurements in compression were also performed using the same Instron Electropuls E10000 load frame. Cylindrical samples (with nominal outer diameter of 1 cm as well as length of 1 cm) were also equilibrated at each target temperature for at least 45 min before the experiment. In a compression control mode, the steady state response (load) to the harmonic excitation (displacement) was measured. At least 50 cycles were considered at each frequency.

Finite element analysis

The topological behavior of the meta-structure was simulated using a 2D linearly elastic finite element formulation by means of the commercial package Abaqus/Standard 6.14 (Dassault Systems). For this purpose, a 2D computational model at similar dimensions of the experimental sample was constructed. Under a displacement control simulation, the bottom of the model was fixed (encastré boundary condition) and the model was subjected to a compressive displacement from the top side. No friction was considered between the loading frame and the top side of the model. The model was compressed up to 15% compressive axial strain.

Supporting Information

The Supporting Information is available free of charge on the ACS Publications website at DOI: 10.1021/ACSAMI.xxxxxx.

Appendix I (Design of the meta-structure of meta-aerogels); Appendix II (Steps involved in the inverse molding technique); Appendix III (Formulation of PIR-PUR wet gels and aerogels); Appendix IV (Figures of merit of the shape-memory effect of straight and meta PIR-PUR aerogels) (PDF)

Movie of cross-sectional slices by Computed Tomography (CT) of a meta-aerogel (MP4)
Movie of the auxetic behavior upon compression of a meta-aerogel during Stage 1 of a thermomechanical cycle (MP4)
Movie of the shape recovery of a meta-aerogel from its temporary auxetic shape by exposure to a temperature stimulus (MP4)

Acknowledgments

For financial support we thank the NSF under award numbers CMMI-1661246, CMMI-1636306, CMMI-1726435, CMMI-1727960 and CMMI-1530603 (sub-contract to MS&T from Tufts University). We also thank Covestro LLC for the generous supply of Desmodur N3300A triisocyanate. S. Malakooti would like to also thank the NASA Postdoctoral Program at the NASA Glenn Research Center, administered by Universities Space Research Association under contract with NASA. H. Lu also thanks the support by the Louis A. Beecherl Jr. Chair.

Conflict of Interest

The authors declare no conflict of interest.

References

(1) Liu, C.; Qin, H.; Mather, P. T. Review of Progress in Shape-Memory Polymers. *J. Mater. Chem.* **2007**, *17* (16), 1543–1558. https://doi.org/10.1039/b615954k.

(2) Lendlein, A.; Jiang, H.; Jünger, O.; Langer, R. Light-Induced Shape-Memory Polymers. *Nature* **2005**, *434* (7035), 879–882. https://doi.org/10.1038/nature03496.

(3) Huang, W. M.; Yang, B.; An, L.; Li, C.; Chan, Y. S. Water-Driven Programmable Polyurethane Shape Memory Polymer: Demonstration and Mechanism. *Appl. Phys. Lett.* **2005**, *86* (11), 1–3. https://doi.org/10.1063/1.1880448.

(4) Han, X.-J.; Dong, Z.-Q.; Fan, M.-M.; Liu, Y.; li, J.-H.; Wang, Y.-F.; Yuan, Q.-J.; Li, B.-J.; Zhang, S. PH-Induced Shape-Memory Polymers. *Macromol. Rapid Commun.* **2012**, *33* (12), 1055–1060. https://doi.org/10.1002/marc.201200153.

(5) Mohr, R.; Kratz, K.; Weigel, T.; Lucka-Gabor, M.; Moneke, M.; Lendlein, A. Initiation of Shape-Memory Effect by Inductive Heating of Magnetic Nanoparticles in Thermoplastic Polymers. *Proc. Natl. Acad. Sci. U. S. A.* **2006**, *103* (10), 3540–3545. https://doi.org/10.1073/pnas.0600079103.

(6) Cianchetti, M.; Laschi, C.; Menciassi, A.; Dario, P. Biomedical Applications of Soft Robotics. *Nature Reviews Materials*. Nature Publishing Group June 1, 2018, pp 143–153. https://doi.org/10.1038/s41578-018-0022-y.

(7) Roche, E. T.; Horvath, M. A.; Wamala, I.; Alazmani, A.; Song, S. E.; Whyte, W.; Machaidze, Z.; Payne, C. J.; Weaver, J. C.; Fishbein, G.; Kuebler, J.; Vasilyev, N. V.; Mooney, D. J.; Pigula, F. A.; Walsh, C. J. Soft Robotic Sleeve Supports Heart Function. *Sci. Transl. Med.* **2017**, *9* (373). https://doi.org/10.1126/scitranslmed.aaf3925.

(8) Yu, X.; Xie, Z.; Yu, Y.; Lee, J.; Vazquez-Guardado, A.; Luan, H.; Ruban, J.; Ning, X.;

Akhtar, A.; Li, D.; Ji, B.; Liu, Y.; Sun, R.; Cao, J.; Huo, Q.; Zhong, Y.; Lee, C. M.; Kim, S. Y.; Gutruf, P.; Zhang, C.; Xue, Y.; Guo, Q.; Chempakasseril, A.; Tian, P.; Lu, W.; Jeong, J. Y.; Yu, Y. J.; Cornman, J.; Tan, C. S.; Kim, B. H.; Lee, K. H.; Feng, X.; Huang, Y.; Rogers, J. A. Skin-Integrated Wireless Haptic Interfaces for Virtual and Augmented Reality. *Nature* **2019**, *575* (7783), 473–479. https://doi.org/10.1038/s41586-019-1687-0.

(9) Kanik, M.; Orguc, S.; Varnavides, G.; Kim, J.; Benavides, T.; Gonzalez, D.; Akintilo, T.; Cem Tasan, C.; Chandrakasan, A. P.; Fink, Y.; Anikeeva, P. Strain-Programmable Fiber-Based Artificial Muscle. *Science (80-.).* **2019**, *365* (6449), 145–150. https://doi.org/10.1126/science.aaw2502.

(10) Alapan, Y.; Karacakol, A. C.; Guzelhan, S. N.; Isik, I.; Sitti, M. Reprogrammable Shape Morphing of Magnetic Soft Machines. *Sci. Adv.* **2020**, *6* (38), 6414–6432. https://doi.org/10.1126/sciadv.abc6414.

(11) Liu, J. A. C.; Gillen, J. H.; Mishra, S. R.; Evans, B. A.; Tracy, J. B. Photothermally and Magnetically Controlled Reconfiguration of Polymer Composites for Soft Robotics. *Sci. Adv.* **2019**, *5* (8), eaaw2897. https://doi.org/10.1126/sciadv.aaw2897.

(12) Hartl, D. J.; Lagoudas, D. C. Aerospace Applications of Shape Memory Alloys. *Proc. Inst. Mech. Eng. Part G J. Aerosp. Eng.* **2007**, *221* (4), 535–552. https://doi.org/10.1243/09544100JAERO211.

(13) Santo, L.; Quadrini, F.; Accettura, A.; Villadei, W. Shape Memory Composites for Self-Deployable Structures in Aerospace Applications. In *Procedia Engineering*; Elsevier Ltd, 2014; Vol. 88, pp 42–47. https://doi.org/10.1016/j.proeng.2014.11.124.

(14) Gall, K.; Yakacki, C. M.; Liu, Y.; Shandas, R.; Willett, N.; Anseth, K. S. Thermomechanics of the Shape Memory Effect in Polymers for Biomedical Applications.

J. Biomed. Mater. Res. - Part A **2005**, *73* (3), 339–348. https://doi.org/10.1002/jbm.a.30296.

(15) Safranski, D. L.; Smith, K. E.; Gall, K. Mechanical Requirements of Shape-Memory Polymers in Biomedical Devices. *Polym. Rev.* **2013**, *53* (1), 76–91. https://doi.org/10.1080/15583724.2012.752385.

(16) Hearon, K.; Wierzbicki, M. A.; Nash, L. D.; Landsman, T. L.; Laramy, C.; Lonnecker, A. T.; Gibbons, M. C.; Ur, S.; Cardinal, K. O.; Wilson, T. S.; Wooley, K. L.; Maitland, D. J. A Processable Shape Memory Polymer System for Biomedical Applications. *Adv. Healthc. Mater.* **2015**, *4* (9), 1386–1398. https://doi.org/10.1002/adhm.201500156.

(17) Soutis, C.; Irving, P. *Polymer Composites in the Aerospace Industry*; Elsevier Inc., 2014. https://doi.org/10.1016/C2013-0-16303-9.

(18) Lendlein, A.; Gould, O. E. C. Reprogrammable Recovery and Actuation Behaviour of Shape-Memory Polymers. *Nature Reviews Materials*. Nature Publishing Group February 1, 2019, pp 116–133. https://doi.org/10.1038/s41578-018-0078-8.

(19) Behl, M.; Kratz, K.; Zotzmann, J.; Nöchel, U.; Lendlein, A. Reversible Bidirectional Shape-Memory Polymers. *Adv. Mater.* **2013**, *25* (32), 4466–4469. https://doi.org/10.1002/adma.201300880.

(20) Pierre, A. C. History of Aerogels. In *Aerogels Handbook*; Springer New York: New York, NY, 2011; pp 3–18. https://doi.org/10.1007/978-1-4419-7589-8_1.

(21) Koebel, M. M.; Rigacci, A.; Achard, P. Aerogels for Superinsulation: A Synoptic View. In *Aerogels Handbook*; Springer New York, 2011; pp 607–633. https://doi.org/10.1007/978-1-4419-7589-8_26.

(22) Lee, J. K.; Gould, G. L.; Rhine, W. Polyurea Based Aerogel for a High Performance

Thermal Insulation Material. *J. Sol-Gel Sci. Technol.* **2009**, *49* (2), 209–220. https://doi.org/10.1007/s10971-008-1861-6.

(23) Pierre, A. C.; Rigacci, A. SiO2 Aerogels. In *Aerogels Handbook*; Springer New York: New York, NY, 2011; pp 21–45. https://doi.org/10.1007/978-1-4419-7589-8_2.

(24) Mandal, C.; Donthula, S.; Rewatkar, P. M.; Sotiriou-Leventis, C.; Leventis, N. Experimental Deconvolution of Depressurization from Capillary Shrinkage during Drying of Silica Wet-Gels with SCF CO2 Why Aerogels Shrink? *J. Sol-Gel Sci. Technol.* **2019**, *92* (3), 662–680. https://doi.org/10.1007/s10971-019-05124-x.

(25) Leventis, N.; Lu, H. Polymer-Crosslinked Aerogels. In *Aerogels Handbook*; Springer New York: New York, NY, 2011; pp 251–285. https://doi.org/10.1007/978-1-4419-7589-8_13.

(26) Leventis, N.; Sotiriou-Leventis, C.; Zhang, G.; Rawashdeh, A.-M. M. Nanoengineering Strong Silica Aerogels. *Nano Lett.* **2002**, *2* (9), 957–960. https://doi.org/10.1021/NL025690E.

(27) Leventis, N. Three-Dimensional Core-Shell Superstructures: Mechanically Strong Aerogels. *Accounts of Chemical Research*. American Chemical Society September 2007, pp 874–884. https://doi.org/10.1021/ar600033s.

(28) Mandal, C.; Donthula, S.; Far, H. M.; Saeed, A. M.; Sotiriou-Leventis, C.; Leventis, N. Transparent, Mechanically Strong, Thermally Insulating Cross-Linked Silica Aerogels for Energy-Efficient Windows. *J. Sol-Gel Sci. Technol.* **2019**, *92* (1), 84–100. https://doi.org/10.1007/s10971-019-05100-5.

(29) Meador, M. A. B. Improving Elastic Properties of Polymer-Reinforced Aerogels. In *Aerogels Handbook*; Springer New York, 2011; pp 315–334. https://doi.org/10.1007/978-1-4419-7589-8_15.

(30) Meador, M. A. B.; Capadona, L. A.; McCorkle, L.; Papadopoulos, D. S.; Nicholas, L. Structure−Property Relationships in Porous 3D Nanostructures as a Function of Preparation Conditions: Isocyanate Cross-Linked Silica Aerogels. *Chem. Mater.* **2007**, *19* (9), 2247–2260. https://doi.org/10.1021/CM070102P.

(31) Lu, H.; Luo, H.; Leventis, N. Mechanical Characterization of Aerogels. In *Aerogels Handbook*; Springer New York: New York, NY, 2011; pp 499–535. https://doi.org/10.1007/978-1-4419-7589-8_22.

(32) **(A)** Sadekar, A. G.; Mahadik, S. S.; Bang, A. N.; Larimore, Z. J.; Wisner, C. A.; Bertino, M. F.; Kalkan, A. K.; Mang, J. T.; Sotiriou-Leventis, C.; Leventis, N. From 'Green' Aerogels to Porous Graphite by Emulsion Gelation of Acrylonitrile. *Chem. Mater.* **2012**, *24* (1), 26–47. https://doi.org/10.1021/cm202975p.; **(B)** Chriti, D.; Raptopoulos, G.; Anyfantis, G. C.; Paraskevopoulou, P. An Extreme Case of Swelling of Mostly Cis - Polydicyclopentadiene by Selective Solvent Absorption—Application in Decontamination and Environmental Remediation . *ACS Appl. Polym. Mater.* **2019**, *1* (7), 1648–1659. https://doi.org/10.1021/acsapm.9b00221.; **(C)** Raptopoulos, G.; Anyfantis, G. C.; Chriti, D.; Paraskevopoulou, P. Synthesis and Structural Characterization of Poly(Dicyclopentadiene) Gels Obtained with a Novel Ditungsten versus Conventional W and Ru Mononuclear Catalysts. *Inorganica Chim. Acta* **2017**, *460*, 69–76. https://doi.org/10.1016/j.ica.2016.09.008.; **(D)** Mohite, D. P.; Mahadik-Khanolkar, S.; Luo, H.; Lu, H.; Sotiriou-Leventis, C.; Leventis, N. Polydicyclopentadiene Aerogels Grafted with PMMA: I. Molecular and Interparticle Crosslinking. *Soft Matter* **2013**, *9* (5), 1516–1530. https://doi.org/10.1039/C2SM26931G.; **(E)** Lee, J. K.; Gould, G. L. Polydicyclopentadiene Based Aerogel: A New Insulation Material. *J. Sol-Gel Sci.*

(33) **(A)** Far, H. M.; Donthula, S.; Taghvaee, T.; Saeed, A. M.; Garr, Z.; Sotiriou-Leventis, C.; Leventis, N. Air-Oxidation of Phenolic Resin Aerogels: Backbone Reorganization, Formation of Ring-Fused Pyrylium Cations, and the Effect on Microporous Carbons with Enhanced Surface Areas. *RSC Adv*. **2017**, *7* (81), 51104–51120. https://doi.org/10.1039/c7ra10958j.; **(B)** Malakooti, S.; Qin, G.; Mandal, C.; Soni, R.; Taghvaee, T.; Ren, Y.; Chen, H.; Tsao, N.; Shiao, J.; Kulkarni, S. S.; Sotiriou-Leventis, C.; Leventis, N.; Lu, H. Low-Cost, Ambient-Dried, Superhydrophobic, High Strength, Thermally Insulating, and Thermally Resilient Polybenzoxazine Aerogels. *ACS Appl. Polym. Mater*. **2019**, *1* (9), 2322–2333. https://doi.org/10.1021/acsapm.9b00408.; **(C)** Mahadik-Khanolkar, S.; Donthula, S.; Sotiriou-Leventis, C.; Leventis, N. Polybenzoxazine Aerogels. 1. High-Yield Room-Temperature Acid-Catalyzed Synthesis of Robust Monoliths, Oxidative Aromatization, and Conversion to Microporous Carbons. *Chem. Mater*. **2014**, *26* (3), 1303–1317. https://doi.org/10.1021/cm403483p.; **(D)** Mulik, S.; Sotiriou-Leventis, C.; Leventis, L. N. Time-Efficient Acid-Catalyzed Synthesis of Resorcinol-Formaldehyde Aerogels. *Chem. Mater*. **2007**, *19* (25), 6138–6144. https://doi.org/10.1021/cm071572m.

(34) **(A)** Meador, M. A. B.; Malow, E. J.; Silva, R.; Wright, S.; Quade, D.; Vivod, S. L.; Guo, H.; Guo, J.; Cakmak, M. Mechanically Strong, Flexible Polyimide Aerogels Cross-Linked with Aromatic Triamine. *ACS Appl. Mater. Interfaces* **2012**, *4* (2), 536–544. https://doi.org/10.1021/am2014635.; **(B)** Guo, H.; Meador, M. A. B.; McCorkle, L.; Quade, D. J.; Guo, J.; Hamilton, B.; Cakmak, M.; Sprowl, G. Polyimide Aerogels Cross-Linked through Amine Functionalized Polyoligomeric Silsesquioxane. *ACS Appl. Mater. Interfaces* **2011**, *3* (2), 546–552. https://doi.org/10.1021/am101123h.; **(C)** Vivod, S. L.;

Meador, M. A. B.; Pugh, C.; Wilkosz, M.; Calomino, K.; McCorkle, L. Toward Improved Optical Transparency of Polyimide Aerogels. *ACS Appl. Mater. Interfaces* **2020**, *12* (7), 8622–8633. https://doi.org/10.1021/acsami.9b17796.

(35) Saeed, A. M.; Wisner, C. A.; Donthula, S.; Majedi Far, H.; Sotiriou-Leventis, C.; Leventis, N. Reuseable Monolithic Nanoporous Graphite-Supported Nanocatalysts (Fe, Au, Pt, Pd, Ni, and Rh) from Pyrolysis and Galvanic Transmetalation of Ferrocene-Based Polyamide Aerogels. *Chem. Mater.* **2016**, *28* (13), 4867–4877. https://doi.org/10.1021/acs.chemmater.6b02364.

(36) **(A)** Taghvaee, T.; Donthula, S.; Rewatkar, P. M.; Majedi Far, H.; Sotiriou-Leventis, C.; Leventis, N. *K*-Index: A Descriptor, Predictor, and Correlator of Complex Nanomorphology to Other Material Properties. *ACS Nano* **2019**, *13* (3), 3677–3690. https://doi.org/10.1021/acsnano.9b00396.; **(B)** Chriti, D.; Raptopoulos, G.; Papastergiou, M.; Paraskevopoulou, P.; Chriti, D.; Raptopoulos, G.; Papastergiou, M.; Paraskevopoulou, P. Millimeter-Size Spherical Polyurea Aerogel Beads with Narrow Size Distribution. *Gels* **2018**, *4* (3), 66. https://doi.org/10.3390/gels4030066.; **(C)** Leventis, N.; Sotiriou-Leventis, C.; Saeed, A. M.; Donthula, S.; Majedi Far, H.; Rewatkar, P. M.; Kaiser, H.; Robertson, J. D.; Lu, H.; Churu, G. Nanoporous Polyurea from a Triisocyanate and Boric Acid: A Paradigm of a General Reaction Pathway for Isocyanates and Mineral Acids. *Chem. Mater.* **2016**, *28* (1), 67–78. https://doi.org/10.1021/acs.chemmater.5b03117.; **(D)** Leventis, N.; Sotiriou-Leventis, C.; Chandrasekaran, N.; Mulik, S.; Larimore, Z. J.; Lu, H.; Churu, G.; Mang, J. T. Multifunctional Polyurea Aerogels from Isocyanates and Water. A Structure-Property Case Study. *Chem. Mater.* **2010**, *22* (24), 6692–6710. https://doi.org/10.1021/cm102891d.; **(E)** Paraskevopoulou, P.; Smirnova, I.; Athamneh,

T.; Papastergiou, M.; Chriti, D.; Mali, G.; Čendak, T.; Chatzichristidi, M.; Raptopoulos, G.; Gurikov, P. Mechanically Strong Polyurea/Polyurethane-Cross-Linked Alginate Aerogels. *ACS Appl. Polym. Mater.* **2020**, *2* (5), 1974–1988. https://doi.org/10.1021/acsapm.0c00162.; **(F)** Malakooti, S.; Hatamleh, M. I.; Zhang, R.; Taghvaee, T.; Miller, M.; Ren, Y.; Xiang, N.; Qian, D.; Sotiriou-Leventis, C.; Leventis, N.; Lu, H. Metamaterial-like Aerogels for Broadband Vibration Mitigation. *Soft Matter* **2021**. https://doi.org/10.1039/d1sm00074h.

(37) Bang, A.; Buback, C.; Sotiriou-Leventis, C.; Leventis, N. Flexible Aerogels from Hyperbranched Polyurethanes: Probing the Role of Molecular Rigidity with Poly(Urethane Acrylates) Versus Poly(Urethane Norbornenes). *Chem. Mater.* **2014**, *26* (24), 6979–6993. https://doi.org/10.1021/cm5031443.

(38) Chidambareswarapattar, C.; McCarver, P. M.; Luo, H.; Lu, H.; Sotiriou-Leventis, C.; Leventis, N. Fractal Multiscale Nanoporous Polyurethanes: Flexible to Extremely Rigid Aerogels from Multifunctional Small Molecules. *Chem. Mater.* **2013**, *25* (15), 3205–3224. https://doi.org/10.1021/cm401623h.

(39) Kanellou, A.; Anyfantis, G.; Chriti, D.; Raptopoulos, G.; Pitsikalis, M.; Paraskevopoulou, P.; Kanellou, A.; Anyfantis, G. C.; Chriti, D.; Raptopoulos, G.; Pitsikalis, M.; Paraskevopoulou, P. Poly(Urethane-Norbornene) Aerogels via Ring Opening Metathesis Polymerization of Dendritic Urethane-Norbornene Monomers: Structure-Property Relationships as a Function of an Aliphatic Versus an Aromatic Core and the Number of Peripheral Norbornene Moieties. *Molecules* **2018**, *23* (5), 1007. https://doi.org/10.3390/molecules23051007.

(40) Donthula, S.; Mandal, C.; Leventis, T.; Schisler, J.; Saeed, A. M.; Sotiriou-Leventis, C.;

Leventis, N. Shape Memory Superelastic Poly(Isocyanurate-Urethane) Aerogels (PIR-PUR) for Deployable Panels and Biomimetic Applications. *Chem. Mater.* **2017**, *29* (10), 4461–4477. https://doi.org/10.1021/acs.chemmater.7b01020.

(41) Donthula, S.; Mandal, C.; Schisler, J.; Leventis, T.; Meador, M. A. B.; Sotiriou-Leventis, C.; Leventis, N. Nanostructure-Dependent Marcus-Type Correlation of the Shape Recovery Rate and the Young's Modulus in Shape Memory Polymer Aerogels. *ACS Appl. Mater. Interfaces* **2018**, *10* (27), 23321–23334. https://doi.org/10.1021/acsami.8b06234.

(42) Malakooti, S.; Rostami, S.; Churu, H. G.; Luo, H.; Clark, J.; Casarez, F.; Rettenmaier, O.; Daryadel, S.; Minary-Jolandan, M.; Sotiriou-Leventis, C.; Leventis, N.; Lu, H. Scalable, Hydrophobic and Highly-Stretchable Poly(Isocyanurate–Urethane) Aerogels. *RSC Adv.* **2018**, *8* (38), 21214–21223. https://doi.org/10.1039/C8RA03085E.

(43) Bertoldi, K.; Vitelli, V.; Christensen, J.; Van Hecke, M. Flexible Mechanical Metamaterials. *Nat. Rev. Mater.* **2017**, *2* (11), 1–11. https://doi.org/10.1038/natrevmats.2017.66.

(44) Zheng, X.; Lee, H.; Weisgraber, T. H.; Shusteff, M.; DeOtte, J.; Duoss, E. B.; Kuntz, J. D.; Biener, M. M.; Ge, Q.; Jackson, J. A.; Kucheyev, S. O.; Fang, N. X.; Spadaccini, C. M. Ultralight, Ultrastiff Mechanical Metamaterials. *Science (80-.).* **2014**, *344* (6190), 1373–1377. https://doi.org/10.1126/science.1252291.

(45) Lakes, R. S. Negative-Poisson's-Ratio Materials: Auxetic Solids. *Annu. Rev. Mater. Res.* **2017**, *47*, 63–81. https://doi.org/10.1146/annurev-matsci-070616-124118.

(46) Evans, K. E.; Alderson, A. Auxetic Materials: Functional Materials and Structures from Lateral Thinking! *Adv. Mater.* **2000**, *12* (9), 617–628. https://doi.org/10.1002/(SICI)1521-4095(200005)12:9<617::AID-ADMA617>3.0.CO;2-3.

(47) Liu, Q. *Literature Review: Materials with Negative Poisson's Ratios and Potential Applications to Aerospace and Defence*; 2006.

(48) Li, T.; Chen, Y.; Hu, X.; Li, Y.; Wang, L. Exploiting Negative Poisson's Ratio to Design 3D-Printed Composites with Enhanced Mechanical Properties. *Mater. Des.* **2018**, *142*, 247–258. https://doi.org/10.1016/j.matdes.2018.01.034.

(49) Overvelde, J. T. B.; Shan, S.; Bertoldi, K. Compaction through Buckling in 2D Periodic, Soft and Porous Structures: Effect of Pore Shape. *Adv. Mater.* **2012**, *24* (17), 2337–2342. https://doi.org/10.1002/adma.201104395.

(50) Babaee, S.; Shim, J.; Weaver, J. C.; Chen, E. R.; Patel, N.; Bertoldi, K. 3D Soft Metamaterials with Negative Poisson's Ratio. *Adv. Mater.* **2013**, *25* (36), 5044–5049. https://doi.org/10.1002/adma.201301986.

(51) SOLIDWORKS 3D CAD | SOLIDWORKS https://www.solidworks.com/product/solidworks-3d-cad (accessed May 4, 2021).

(52) Choong, Y. Y. C.; Tan, H. W.; Patel, D. C.; Choong, W. T. N.; Chen, C. H.; Low, H. Y.; Tan, M. J.; Patel, C. D.; Chua, C. K. The Global Rise of 3D Printing during the COVID-19 Pandemic. *Nature Reviews Materials*. Nature Research September 1, 2020, pp 637–639. https://doi.org/10.1038/s41578-020-00234-3.

(53) Chua, C. K.; Leong, K. F. *3D Printing and Additive Manufacturing: Principles and Applications: The 5th Edition of Rapid Prototyping: Principles and Applications*; World Scientific Publishing Co., 2017. https://doi.org/10.1142/10200.

(54) Zhu, C.; Han, T. Y. J.; Duoss, E. B.; Golobic, A. M.; Kuntz, J. D.; Spadaccini, C. M.; Worsley, M. A. Highly Compressible 3D Periodic Graphene Aerogel Microlattices. *Nat. Commun.* **2015**, *6* (1), 1–8. https://doi.org/10.1038/ncomms7962.

(55) Zhang, Q.; Zhang, F.; Medarametla, S. P.; Li, H.; Zhou, C.; Lin, D. 3D Printing of Graphene Aerogels. *Small* **2016**, *12* (13), 1702–1708. https://doi.org/10.1002/smll.201503524.

(56) Saeed, S.; Al Soubaihi, R. M.; White, L. S.; Bertino, M. F.; Saoud, K. M. Rapid Fabrication of Cross-Linked Silica Aerogel by Laser Induced Gelation. *Microporous Mesoporous Mater.* **2016**, *221*, 245–252. https://doi.org/10.1016/j.micromeso.2015.09.012.

(57) Zhao, S.; Siqueira, G.; Drdova, S.; Norris, D.; Ubert, C.; Bonnin, A.; Galmarini, S.; Ganobjak, M.; Pan, Z.; Brunner, S.; Nyström, G.; Wang, J.; Koebel, M. M.; Malfait, W. J. Additive Manufacturing of Silica Aerogels. *Nature* **2020**, *584* (7821), 387–392. https://doi.org/10.1038/s41586-020-2594-0.

(58) Che, K.; Yuan, C.; Qi, H. J.; Meaud, J. Viscoelastic Multistable Architected Materials with Temperature-Dependent Snapping Sequence †. *2492 | Soft Matter* **2018**, *14*, 2492. https://doi.org/10.1039/c8sm00217g.

(59) Joo, P.; Yao, Y.; Teo, N.; Jana, S. C. Modular Aerogel Brick Fabrication via 3D-Printed Molds. *Addit. Manuf.* **2021**, *46*, 102059. https://doi.org/10.1016/j.addma.2021.102059.

(60) Turner, B. N.; Strong, R.; Gold, S. A. A Review of Melt Extrusion Additive Manufacturing Processes: I. Process Design and Modeling. *Rapid Prototyping Journal*. Emerald Group Publishing Ltd. 2014, pp 192–204. https://doi.org/10.1108/RPJ-01-2013-0012.

(61) Tanikella, N. G.; Wittbrodt, B.; Pearce, J. M. Tensile Strength of Commercial Polymer Materials for Fused Filament Fabrication 3D Printing. *Addit. Manuf.* **2017**, *15*, 40–47. https://doi.org/10.1016/j.addma.2017.03.005.

(62) Defeyt, C.; Langenbacher, J.; Rivenc, R. Polyurethane Coatings Used in Twentieth Century Outdoor Painted Sculptures. Part I: Comparative Study of Various Systems by Means of ATR-FTIR Spectroscopy. *Herit. Sci.* **2017**, *5* (1), 11. https://doi.org/10.1186/s40494-017-0124-7.

(63) Silverstein, R. M.; Webster, F. X.; Kiemle, D. J. *Spectrometric Identification of Organic Compounds.*; John Wiley & Sons, 2005.

(64) McCarthy, S. J.; Meijs, G. F.; Mitchell, N.; Gunatillake, P. A.; Heath, G.; Brandwood, A.; Schindhelm, K. In-Vivo Degradation of Polyurethanes: Transmission-FTIR Microscopic Characterization of Polyurethanes Sectioned by Cryomicrotomy. *Biomaterials* **1997**, *18* (21), 1387–1409. https://doi.org/10.1016/S0142-9612(97)00083-5.

(65) Leventis, N.; Sotiriou-Leventis, C.; Chandrasekaran, N.; Mulik, S.; Larimore, Z. J.; Lu, H.; Churu, G.; Mang, J. T. Multifunctional Polyurea Aerogels from Isocyanates and Water. A Structure-Property Case Study. *Chem. Mater.* **2010**, *22* (24), 6692–6710. https://doi.org/10.1021/cm102891d.

(66) Malakooti, S.; Qin, G.; Mandal, C.; Soni, R.; Taghvaee, T.; Ren, Y.; Chen, H.; Tsao, N.; Shiao, J.; Kulkarni, S. S.; Sotiriou-Leventis, C.; Leventis, N.; Lu, H. Low-Cost, Ambient-Dried, Superhydrophobic, High Strength, Thermally Insulating, and Thermally Resilient Polybenzoxazine Aerogels. *ACS Appl. Polym. Mater.* **2019**, *1* (9), 2322–2333. https://doi.org/10.1021/acsapm.9b00408.

(67) 3D Hubs | On-demand Manufacturing: Quotes in Seconds, Parts in Days https://www.3dhubs.com/ (accessed May 4, 2021).